Vision-Based Control of a Knuckle Boom Crane With Online Cable Length Estimation

Geir Ole Tysse, *Member, IEEE*, Andrej Cibicik, *Member, IEEE*, and Olav Egeland, *Senior Member, IEEE*

***Abstract*—A vision-based controller for a knuckle boom crane is presented. The controller is used to control the motion of the crane tip, and at the same time, compensate for payload oscillations. The oscillations of the payload are measured with three cameras that are fixed to the crane king, and are used to track two spherical markers fixed to the payload cable. Based on color and size information, each camera identifies the image points corresponding to the markers. The payload angles are then determined using linear triangulation of the image points. An extended Kalman filter is used for the estimation of payload angles and angular velocity. The length of the payload cable is also estimated using the least-squares technique with projection. The crane is controlled by a linear cascade controller where the inner control loop is designed to damp out the pendulum oscillation, and the crane tip is controlled by the outer loop. The control variable of the controller is the commanded crane tip acceleration, which is converted to a velocity command using a velocity loop. The performance of the control system is studied experimentally using a scaled laboratory version of a knuckle boom crane.**

***Index Terms*—Control, crane, estimation, vision.**

I. Introduction

CRANES are important in a wide range of operations, both onshore and offshore. Crane hoisting operations may be associated with high risk due to the motion of a heavy payload. The landing of the payload is especially critical, since underestimation of the payload motion may lead to damage of equipment and injuries to personnel on the landing site. In addition, the knowledge of the vertical position of the payload in relation to the landing site is necessary. Currently, most of the cranes are driven manually by an operator, and without automation for suppressing the sway of the payload. Automatic control of cranes may contribute to the safety of crane operations and reduction of delays. In this article, we present a mechatronic system including a method for the estimation of the crane payload motion using a vision-based system, a controller for suppressing the payload sway, and a procedure for cable length estimation using an adaptive law.

Crane control has been an active area of research during the last decades [1], [2]. One approach is open-loop control laws. This includes input shaping, which was studied in [3], and feedforward techniques [4]. Such methods do not require a feedback signal and can be effective, however, they require that the model of the system is sufficiently accurate. Another approach is closed-loop methods that are less sensitive to modeling errors and noise. A number of energy-based controllers for damping the payload oscillations have been proposed for overhead cranes, which were modeled as cart-payload systems [5]–[9].

A model predictive controller (MPC) is another type of a closed-loop controller that has been used in crane control by several authors. MPC was used for controlling a one-degree-of-freedom (1-DoF) trolley with a pendulum in [10] and [11]. In [12] and [13], a real-time MPC was proposed for a linearized model of a mobile harbor crane, where the luffing and slewing motion were controlled. The reader can refer to the review papers [1] and [2], where crane control strategies are extensively discussed.

A knuckle boom crane has a kinematic structure which is similar to a robotic manipulator, which means that results from robot control can be adapted to the control of knuckle boom cranes. One example of this is 2-D cameras, which are widely used in robotics. Vision allows a robotic system to obtain geometrical information from the surrounding environment to be used for motion planning and control [14]. In visual servoing, the end-effector is controlled relative to a target using visual features extracted from one or several cameras. Early work in this field is well covered in [15]. There are mainly two different visual servoing approaches: image-based visual servoing and position-based visual servoing. In image-based visual servoing [16], the error is defined in the 2-D image space, and in position-based visual servoing [17] the error is defined in the 3-D Cartesian space. Comparison of these methods is found e.g., in [18]. A challenge in position-based visual servoing is that the information about metric distances is lost in the camera projection [19]. Stereo vision is one of the approaches that can be used for recovering of metric distances [20]. In [21], the authors used epipolar geometry for two cameras with a nonlinear minimization technique for recovering the metric distances. In [22], a two-view bundle adjustment approach for visual navigation was presented. The

Manuscript received October 24, 2019; revised April 8, 2020; accepted September 8, 2020. Date of publication September 18, 2020; date of current version February 16, 2021. Recommended by Technical Editor Pinhas Ben-Tzvi and Senior Editor Xiang Chen. The work was supported by the Norwegian Research Council, SFI Offshore Mechatronics, under Project 237896. *(Corresponding author: Andrej Cibicik.)*

The authors are with the Department of Mechanical and Industrial Engineering, Norwegian University of Science and Technology, NO-7465 Trondheim, Norway (e-mail: geir.o.tysse@ntnu.no; andrej.cibicik@ntnu.no; olav.egeland@ntnu.no).

Color versions of one or more of the figures in this article are available online at https://ieeexplore.ieee.org.

Digital Object Identifier 10.1109/TMECH.2020.3024637

3-D scene points can be extracted from the scene objects, which are viewed as image correspondences. A correspondence is a pair of corresponding features in different images that represent the same scene object. A method for determining the 3-D position of points from correspondences is called triangulation, which was solved for the two-view problem in [23]. Review of stereo vision for tracking can be found in [24]–[26]. In the case of a three-view configuration, the accuracy of estimates can be improved [27]–[29].

Adaptive parameter estimation and system identification have been studied for models with unknown parameters in [30] and [31]. Algorithms based on projection, least-squares and gradient search have been widely used, where unknown parameters were estimated using adaptive laws. In [32] and [33], the authors discussed different adaptive estimation of time-varying parameter approaches in nonlinear systems. Practical examples of the application of adaptive real-time parameter estimation for robotic systems are given in [34] and [35].

In this article, we present a vision-based control of a knuckle boom crane with online cable length estimation. The measurements of the payload cable orientation angles are obtained by a sensor configuration where three cameras are rigidly attached to the crane king, which is a new sensor arrangement for crane control. The cameras are used to track the position of two spherical markers attached to the payload cable, where the color and size information of the markers is used. We implement the direct linear transformation procedure, which was given for stereo vision in [23], for a three-camera case to increase the accuracy of the measurements. The extended Kalman filter is used to estimate the orientation angles and angular velocities of the payload. A typical assumption in the crane control papers is that the cable length is known, although, in practice, it may not be the case. Estimation of the cable length is done with the least-squares technique with projection based on an adaptive law. The suggested linear cascade controller damps out the payload oscillations and controls the position of the crane tip. The direct control output is the commanded acceleration of the crane tip, which is converted to the velocity signal, which is a common type of control input for cranes, by the velocity loop [36]. The performance of the proposed system is studied experimentally using a scaled laboratory version of a knuckle boom crane and realistic geometry of the payload. Although knuckle boom cranes are widely used for marine vessels, there are little experimental results on automatic control of this type of cranes in the research literature.

The main contributions of this article are summarized as follows.

1) The proposed scheme is designed and experimentally verified for a knuckle boom crane using the velocity control inputs, while the vast majority of the existing methods are using force/torque control, or deal with the other types of cranes.
2) In the presented problem, both the controller, estimator of the pendulum states, and cable length estimator are all dependent on inputs from each other. We address the problem by proposing and experimentally testing a scheme where the controller, state estimator, and cable length estimator are interconnected (see Fig. 1).

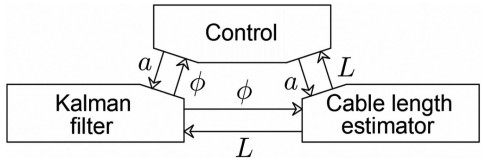

Fig. 1. Communication between the controller, the extended Kalman filter, and the cable length estimator. The signals are denoted as follows: a are the commanded control accelerations, ϕ are the estimates of the payload states, and L is the estimate of the cable length.

3) We propose a cost-efficient visual measurement system, which is new in control of knuckle boom cranes.
4) The proposed cascade controller is simple and intuitive to tune, while it showed to be more efficient for the proposed problem compared to the linear quadratic regulator (LQR) controller and robust extra insensitive (EI) input shaper. It is also more computationally efficient, as it does not require a new optimization (or input generation) for every new cable length estimate.

The rest of this article is organized as follows. In Section II, the knuckle boom crane system is presented, as well as necessary kinematic and dynamic derivations are given. In Section III, the vision-based payload motion estimator is discussed, while in Section IV, the procedure for cable length estimation is presented. The controller for the crane is derived in Section V. The experimental results are given in Section VI, and finally, Section VII concludes this article.

II. Knuckle Boom Crane With Payload

A. System Description

In this article, we consider a small-scale knuckle boom crane with a camera-based sensor package, as shown in Fig. 2. The crane has three actuated DoF. The first actuated DoF is the slewing joint (1), which enables the crane king (4) to rotate about the vertical axis. The second actuated DoF is the extension of the linear actuator (2), which actuates the luffing of the inner boom (5). The third actuated DoF is the extension of the linear actuator (3), which is luffing the outer boom (6). The crane payload (9) is suspended from the crane tip by the cable (7). The payload used in the experiments is a hollow box with mass $m = 12.7\text{kg}$ and the dimensions are $223 \times 223 \times 241$ mm. Two spherical markers (8) are attached to the cable (7). Three 2-D cameras (10) are attached to the crane king (4), such that the cameras rotate with the slew motion of the crane.

B. Crane Kinematics

Consider the mechanical crane system given in Fig. 3 with the parameter values given in Table I. We model the crane as an open-chain kinematic system, where the kinematic relations between the extensions of linear actuators and the joint rotations are defined. The crane pedestal is defined as Body 0, the king is Body 1, the inner boom is Body 2, and the outer boom is Body 3 and Body 4. Each rigid Body i has a body-fixed frame i. It is noted that frame 0 is also the inertial frame. The length of Body i is denoted l_i. The configuration of the system is defined by the

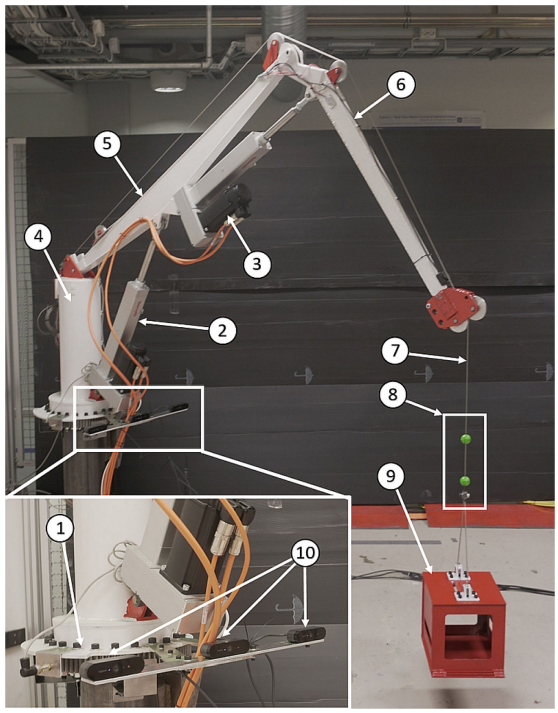

Fig. 2. Small-scale knuckle boom crane with a vision-based sensor—(1) slew joint q_1, (2) linear actuator q_2, (3) linear actuator q_3, (4) crane king, (5) inner boom, (6) outer boom, (7) cable, (8) spherical markers, (9) payload, and (10) 2-D cameras.

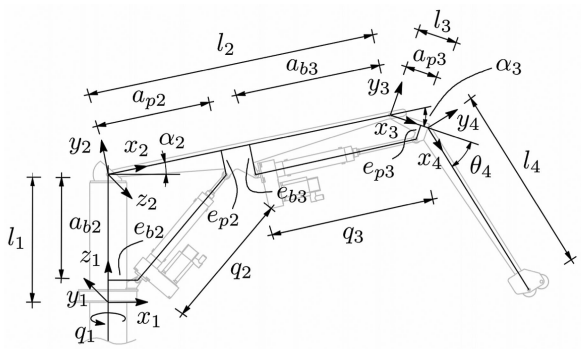

Fig. 3. Geometry of the knuckle boom crane.

vector of generalized coordinates

$$\boldsymbol{q} = \begin{bmatrix} \boldsymbol{q}_c^{\mathrm{T}} & \phi_x & \phi_y \end{bmatrix}^{\mathrm{T}} \tag{1}$$

where $\boldsymbol{q}_c = [q_1, q_2, q_3]^{\mathrm{T}}$ is the crane configuration vector and ϕ_x, ϕ_y are the payload angles.

The rotation matrix from frame 0 to frame 1 is $\boldsymbol{R}_1^0 = \boldsymbol{R}_x(\pi)\boldsymbol{R}_z(-\frac{\pi}{2})\boldsymbol{R}_z(q_1)$. The rotation matrix from frame 1 to frame 2 is $\boldsymbol{R}_2^1 = \boldsymbol{R}_x(\frac{\pi}{2})\boldsymbol{R}_z(\alpha_2(q_2))$. The rotation matrix from frame 2 to frame 3 is $\boldsymbol{R}_3^2 = \boldsymbol{R}_z(\alpha_3(q_3))$. The rotation matrix from frame 3 to frame 4 is $\boldsymbol{R}_4^3 = \boldsymbol{R}_z(\theta_4)$. The origin of frame 5 is attached to the crane tip, but the frame has the same orientation as the inertial frame, that is $\boldsymbol{R}_5^0 = \boldsymbol{I}$. The rotation matrix from frame 5 to frame 6 is $\boldsymbol{R}_6^5 = \boldsymbol{R}_x(\phi_x)\boldsymbol{R}_y(\phi_y)$, which also

TABLE I
GEOMETRICAL PARAMETERS OF THE CRANE

Term	Value	Term	Value	Term	Value
l_1	0.711 m	e_{b2}	0.154 m	a_{p3}	0.167 m
l_2	1.500 m	a_{p2}	0.600 m	e_{p3}	0.076 m
l_3	0.205 m	e_{p2}	0.130 m	θ_4	−39.4 deg
l_4	0.992 m	a_{b3}	0.750 m		
a_{b2}	0.550 m	e_{b3}	0.160 m		

leads to $\boldsymbol{R}_6^0 = \boldsymbol{R}_x(\phi_x)\boldsymbol{R}_y(\phi_y)$. Frame 6 is body-fixed frame of the payload cable. The matrices $\boldsymbol{R}_x, \boldsymbol{R}_y, \boldsymbol{R}_z \in \mathrm{SO}(3)$ are the orthogonal rotation matrices about the x-, y-, and z-axes, respectively [37]. The rotation angle $\alpha_i(q_i)$ from frame $i-1$ to frame i is defined as

$$\alpha_i(q_i) = \arccos \frac{q_i^2 - b_{i1}^2 - b_{i2}^2}{-2b_{i1}b_{i2}} + \arctan \frac{e_{bi}}{a_{bi}} + \arctan \frac{e_{pi}}{a_{pi}} - c_i, \quad \text{for } i = 2, 3 \tag{2}$$

where $c_2 = 0.5\pi$, $c_3 = \pi$, $b_{i1}^2 = a_{bi}^2 + e_{bi}^2$, $b_{i2}^2 = a_{pi}^2 + e_{pi}^2$ and $a_{bi}, a_{pi}, e_{bi}, e_{pi}$ are defined in Fig. 3. The rates of the orientation angles (2) can be found by time differentiation, which gives $\dot{\alpha}_i = \dot{q}_i \, \partial\alpha_i/\partial q_i$. The relative angular velocities between the frames are given as

$$\boldsymbol{\omega}_{01}^1 = \dot{q}_1 \boldsymbol{z}_1^1, \quad \boldsymbol{\omega}_{i-1,i}^i = \dot{\alpha}_i \boldsymbol{z}_i^i, \quad \text{for } i = 2, 3 \tag{3}$$

where the joint i rotation axis is $\boldsymbol{z}_i^i = [0, 0, 1]^{\mathrm{T}}$ and the orientation between frames 3 and 4 is constant, i.e., $\boldsymbol{\omega}_{34}^4 = \boldsymbol{0}$. The distance vectors between the origins of the frames given in the coordinate of the local frame are

$$\boldsymbol{p}_{01}^0 = \boldsymbol{0}, \quad \boldsymbol{p}_{12}^1 = \begin{bmatrix} 0 & 0 & l_1 \end{bmatrix}^{\mathrm{T}}$$
$$\boldsymbol{p}_{i,i+1}^i = \begin{bmatrix} l_i & 0 & 0 \end{bmatrix}^{\mathrm{T}}, \quad \text{for } i = 2, 3, 4. \tag{4}$$

Then the distance vector from the origin of frame i to the origin of frame 5 given in the coordinates of 0 is found as

$$\boldsymbol{p}_{i5}^0 = \sum_{k=i}^{4} \left[\prod_{j=1}^{k} \boldsymbol{R}_j^{j-1} \right] \boldsymbol{p}_{k,k+1}^k, \quad \text{for } i = 1, 2, 3. \tag{5}$$

The linear velocity of the origin of frame 5 can be given in the coordinates of the inertial frame in terms of the Jacobian $\boldsymbol{J}$ as

$$\boldsymbol{v}_{05}^0 = \boldsymbol{J}\dot{\boldsymbol{q}}_c. \tag{6}$$

The Jacobian in (6) maps, the rates of the generalized coordinates of the crane to the linear velocity of the crane tip and is given as

$$\boldsymbol{J} = \begin{bmatrix} \hat{\boldsymbol{z}}_1^0 \boldsymbol{p}_{15}^0 & \hat{\boldsymbol{z}}_2^0 \boldsymbol{p}_{25}^0 & \hat{\boldsymbol{z}}_3^0 \boldsymbol{p}_{35}^0 \end{bmatrix} \begin{bmatrix} 1 & 0 & 0 \\ 0 & \frac{\partial\alpha_2}{\partial q_2} & 0 \\ 0 & 0 & \frac{\partial\alpha_3}{\partial q_3} \end{bmatrix} \tag{7}$$

where $\hat{\cdot}$ denotes the skew-symmetric form of a vector, while $\boldsymbol{p}_{i5}^0$ is given by (5), and $\boldsymbol{z}_1^0 = \boldsymbol{R}_1^0 \boldsymbol{z}_1^1$, $\boldsymbol{z}_2^0 = \boldsymbol{R}_2^0 \boldsymbol{z}_2^2$ and $\boldsymbol{z}_3^0 = \boldsymbol{R}_3^0 \boldsymbol{z}_3^3$.

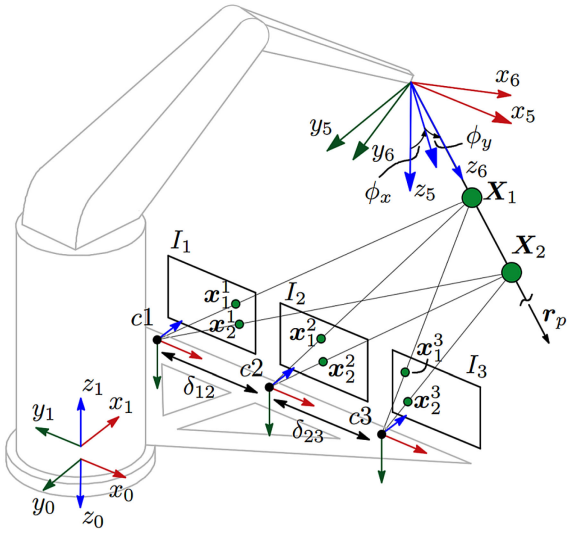

Fig. 4. Three cameras are installed on a rack, which is rigidly attached to the king of the crane. The spherical markers are projected as pixels into the image planes of the cameras.

C. Payload Modeling

The crane payload is modeled as a spherical pendulum, where the mass of the cable is neglected, and the mass m of the payload is lumped at the end of the cable of length L. The acceleration of gravity is g. The payload has a body-fixed frame 6, which has the origin coinciding with the origin of frame 5. The equations of motion for a spherical pendulum can explicitly be written as [38]

$$\begin{aligned}\ddot{\phi}_x c_y + \omega_0^2 s_x &= 2\dot{\phi}_x \dot{\phi}_y s_y + \dot{v}_y c_x / L \\ \ddot{\phi}_y + \omega_0^2 c_x s_y &= -\dot{\phi}_x^2 s_y c_y - (\dot{v}_x c_y + \dot{v}_y s_x s_y)/L \end{aligned} \quad (8)$$

where the square of the eigenfrequency is $\omega_0^2 = g/L$, while $\dot{v}_x = \ddot{x}_5$, $\dot{v}_y = \ddot{y}_5$, $s_i = \sin\phi_i$ and $c_i = \cos\phi_i$.

III. Estimation of Payload Motion

A. Vision

In this section, we present the procedure for the determination of the payload orientation angles (ϕ_x, ϕ_y) (see Fig. 4) using three-camera measurements. The measured angles are further used in combination with an extended Kalman filter for estimation of the orientation angles and angular velocities. Each camera i has a camera-fixed frame ci.

Consider two points $\boldsymbol{X}_1 = [X_1, Y_1, Z_1]^{\mathrm{T}}$ and $\boldsymbol{X}_2 = [X_2, Y_2, Z_2]^{\mathrm{T}}$ given in Fig. 4, where each of the points is located in the center of a spherical marker. These points can be given relative to frame $c1$ of camera 1, and expressed in the coordinates of the inertial frame as

$$\boldsymbol{X}_j = \boldsymbol{p}_{c1,5}^0 + \boldsymbol{R}_6^0 \Delta_j \boldsymbol{e}_3, \quad \text{for } j = 1, 2 \quad (9)$$

where $\boldsymbol{p}_{c1,5}^0 = \boldsymbol{p}_{05}^0 - \boldsymbol{p}_{0,c1}^0$ is the vector from the origin of frame $c1$ to the origin of frame 5, and $\boldsymbol{R}_6^0 \Delta_j \boldsymbol{e}_3$ is the position of the marker relative to the crane tip. The term Δ_j is the scalar distance from the origin of frame 5 to the center of a spherical marker and $\boldsymbol{e}_3 = [0, 0, 1]^{\mathrm{T}}$. Consider a line through the points $\boldsymbol{X}_j$ with a normalized direction vector $\boldsymbol{r}_p = [r_x, r_y, r_z]^{\mathrm{T}}$ given as

$$\boldsymbol{r}_p = \frac{\boldsymbol{X}_2 - \boldsymbol{X}_1}{\Delta_2 - \Delta_1} = \boldsymbol{R}_6^0 \boldsymbol{e}_3 = \begin{bmatrix} s_y & -s_x c_y & c_x c_y \end{bmatrix}^{\mathrm{T}}. \quad (10)$$

The points $\boldsymbol{X}_j$ are seen in the image plane I_i of camera i as pixels $\boldsymbol{x}_j^i = [u_j^i, v_j^i]^{\mathrm{T}}$. The coordinates of the pixels in the image plane can be obtained as

$$\tilde{\boldsymbol{x}}_j^i = \boldsymbol{P}_i \tilde{\boldsymbol{X}}_j \quad (11)$$

where the tilde notation $\tilde{\cdot}$ is a homogeneous representation of a vector [37]. The method for tracking and extracting the points $\boldsymbol{x}_j^i$ can be summed up by the following steps:

1) blur image I_i by a Gaussian function;
2) convert I_i from the RBG to the HSV color space and define a binary image $\hat{I}_i$ based on the range of pixel values in I_i;
3) apply the morphology operators erosion and dilation to $\hat{I}_i$;
4) enclose objects by circles and remove objects that are outside the range of desired radii;
5) find raw image moments of the objects and calculate the centroids $\boldsymbol{x}_1^i = [u_1^i, v_1^i]^{\mathrm{T}}$ and $\boldsymbol{x}_2^i = [u_2^i, v_2^i]^{\mathrm{T}}$ where $v_2^i > v_1^i$.

The camera matrix $\boldsymbol{P}_i$ for camera i in (11) is defined as

$$\boldsymbol{P}_i = \boldsymbol{K}_i \left[\boldsymbol{R}_0^{ci} \,|\, \boldsymbol{t}_{ci,c1}^{ci} \right] \quad (12)$$

where the rotation matrix from the inertial frame to frame ci is given as $\boldsymbol{R}_{ci}^0 = \boldsymbol{R}_1^0 \boldsymbol{R}_x(\pi/2)^{\mathrm{T}} \boldsymbol{R}_y(\pi/2)$ for $i = 1, 2, 3$ and $\boldsymbol{K}_i$ is the camera calibration matrix for camera i [37]. The constant translation vectors from frame ci to frame $c1$, expressed in the coordinates of ci are $\boldsymbol{t}_{c2,c1}^{c2} = -\delta_{12}\boldsymbol{e}_1$ and $\boldsymbol{t}_{c3,c1}^{c3} = -(\delta_{12} + \delta_{23})\boldsymbol{e}_1$, where $\boldsymbol{e}_1 = [1, 0, 0]^{\mathrm{T}}$. The terms in (11) will satisfy the equality $\hat{\tilde{\boldsymbol{x}}}_j^i \boldsymbol{P}_i \tilde{\boldsymbol{X}}_j = \boldsymbol{0}$. Define $\bar{\boldsymbol{A}}_j^i = \hat{\tilde{\boldsymbol{x}}}_j^i \boldsymbol{P}_i \in \mathbb{R}^{3\times 4}$, and let $\boldsymbol{A}_j^i \in \mathbb{R}^{2\times 4}$ denote the matrix which is formed by removing the last row of $\bar{\boldsymbol{A}}_j^i$. Then $\boldsymbol{A}_j^i \tilde{\boldsymbol{X}}_j = \boldsymbol{0}$, where

$$\boldsymbol{A}_j^i = \begin{bmatrix} v_j^i \boldsymbol{P}_i^3 - \boldsymbol{P}_i^2 \\ \boldsymbol{P}_i^1 - u_j^i \boldsymbol{P}_i^3 \end{bmatrix} \quad (13)$$

and $\boldsymbol{P}_i^k$ denotes the kth row of $\boldsymbol{P}_i$. Similarly as in (13), the equality $\boldsymbol{A}_j \tilde{\boldsymbol{X}}_j = \boldsymbol{0}$ can be formulated taking into account measurement from all the cameras, where the matrix $\boldsymbol{A}_j$ is given as

$$\boldsymbol{A}_j = \begin{bmatrix} (\boldsymbol{A}_j^1)^{\mathrm{T}} & (\boldsymbol{A}_j^2)^{\mathrm{T}} & (\boldsymbol{A}_j^3)^{\mathrm{T}} \end{bmatrix}^{\mathrm{T}}. \quad (14)$$

The constraint equation $\boldsymbol{A}_j \tilde{\boldsymbol{X}}_j = \boldsymbol{0}$ requires that the matrices $\boldsymbol{A}_j \in \mathbb{R}^{6\times 4}$ have rank 3 if the points $\boldsymbol{x}_j^i$ are exact without noise. Singular value decomposition of $\boldsymbol{A}_j$ gives

$$\boldsymbol{A}_j = \sum_{k=1}^{4} \sigma_k^j \boldsymbol{u}_k^j (\boldsymbol{\nu}_k^j)^{\mathrm{T}} \quad (15)$$

where $\sigma_4^j = 0$ if the points $\boldsymbol{x}_j^i$ are exact without noise and $\sigma_4^j > 0$ if the points are noisy. The measurements $\bar{\boldsymbol{X}}_j$ of the actual points

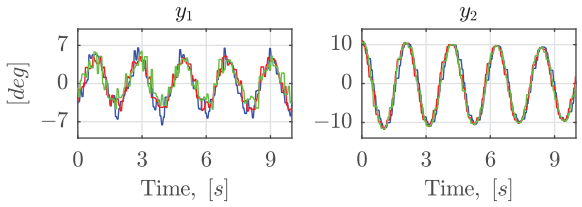

Fig. 5. Measurement (y_1, y_2) of the pendulum orientation angles (ϕ_x, ϕ_y) with different light conditions. The blue lines illustrates the measurements (y_1, y_2) with intensity 330 lx, the red lines illustrates the measurements with intensity 79 lx and the green lines illustrates the measurements with intensity 60 lx. The intensities where measured at the spherical marker $\boldsymbol{X}_1$.

$\boldsymbol{X}_j$ are given by

$$\bar{\tilde{\boldsymbol{X}}}_j = \lambda^j \boldsymbol{\nu}_4^j \tag{16}$$

where $\lambda^j \neq 0$ are scaling factors and $\boldsymbol{\nu}_4^j = [X_j, Y_j, Z_j, 1]^{\mathrm{T}}/\lambda^j$. The measurement $\bar{\boldsymbol{r}}_p = [\bar{r}_x, \bar{r}_y, \bar{r}_z]^{\mathrm{T}}$ of the direction vector $\boldsymbol{r}_p$ is given by

$$\bar{\boldsymbol{r}}_p = (\bar{\boldsymbol{X}}_2 - \bar{\boldsymbol{X}}_1)/\|\bar{\boldsymbol{X}}_2 - \bar{\boldsymbol{X}}_1\|_2. \tag{17}$$

The measurement $\boldsymbol{y} = [y_1, y_2]^{\mathrm{T}}$ of the pendulum orientation angles (ϕ_x, ϕ_y) is then

$$y_1 = \arctan\left[-\frac{\bar{r}_y}{\bar{r}_z}\right], \quad y_2 = \arctan\left[\frac{\bar{r}_x}{(\bar{r}_y^2 + \bar{r}_z^2)^{1/2}}\right] \tag{18}$$

where (10) is used. This solution is based on the direct linear transformation algorithm in [23]. The performance of the vision system in different light conditions is illustrated in Fig. 5. As seen in the figure, the performance of the vision system was satisfactory in the intensity range 60–330 lx. In addition to the results illustrated in the figure, there was run a test with intensity 49 lx where the vision system was not able to track the spherical markers.

It is noted that it would have been sufficient to use two cameras in a stereo arrangement to measure the angle of the cable. In that case, the matrix $\boldsymbol{A}_j$ in (14) would be $\boldsymbol{A}_j = [(\boldsymbol{A}_j^1)^{\mathrm{T}}, (\boldsymbol{A}_j^2)^{\mathrm{T}}]^{\mathrm{T}}$, which would give a sufficient number of conditions on the unknowns to compute the marker positions. In this article, we have decided to use one additional camera. The motivation for this is that it provides additional constraints for the determination of the positions of the markers, which will improve the accuracy. It was seen in the experiments that this lead to a good performance of the camera system. Moreover, the resulting increase in computational cost is modest. As an alternative to this, we could have used two cameras of higher accuracy.

B. Extended Kalman Filter

Consider the state vector given as

$$\boldsymbol{z} = \begin{bmatrix} \phi_x & \phi_y & \dot{\phi}_x & \dot{\phi}_y & n_x & n_y \end{bmatrix}^{\mathrm{T}} \tag{19}$$

where ϕ_i and $\dot{\phi}_i$ are the pendulum orientation angles and angular velocities, while n_i are the bias states due to calibration error. The input vector is given as $\boldsymbol{a} = [\dot{v}_x, \dot{v}_y]^{\mathrm{T}}$, where $\dot{v}_x$ and $\dot{v}_y$ are

Algorithm 1: Extended Kalman Filter Implementation.

$k = 1$, $\hat{\boldsymbol{z}}_{k-1} = \hat{\boldsymbol{z}}_0$, $\hat{\boldsymbol{P}}_{k-1} = \hat{\boldsymbol{P}}_0$
loop
  $\bar{\boldsymbol{z}}_k = \boldsymbol{f}_{k-1}(\hat{\boldsymbol{z}}_{k-1}, \boldsymbol{a}_{k-1}, L)$
  $\bar{\boldsymbol{P}}_k = \boldsymbol{F}_{k-1}\hat{\boldsymbol{P}}_{k-1}\boldsymbol{F}_{k-1}^{\mathrm{T}} + \boldsymbol{Q}$
  $\boldsymbol{K}_k = \bar{\boldsymbol{P}}_k\boldsymbol{H}^{\mathrm{T}}(\boldsymbol{R} + \boldsymbol{H}\bar{\boldsymbol{P}}_k\boldsymbol{H}^{\mathrm{T}})^{-1}$
  $\hat{\boldsymbol{z}}_k = \bar{\boldsymbol{z}}_k + \boldsymbol{K}_k(\boldsymbol{y}_k - \boldsymbol{H}\bar{\boldsymbol{z}}_k)$
  $\hat{\boldsymbol{P}}_k = (\boldsymbol{I} - \boldsymbol{K}_k\boldsymbol{H})\bar{\boldsymbol{P}}_k$
  $k = k + 1$
end loop

the crane tip accelerations in x- and y-directions with respect to the inertial frame. The spherical pendulum dynamics are assumed to be imposed by the white process noise $\boldsymbol{w}$ such that it can be written as a nonlinear stochastic system

$$\dot{\boldsymbol{z}} = \boldsymbol{f}(\boldsymbol{z}, \boldsymbol{a}, L) + \boldsymbol{w} \tag{20}$$

where $\boldsymbol{f}(\boldsymbol{z}, \boldsymbol{a}, L)$ is given by (8) and the bias error $\boldsymbol{n} = [n_x, n_y]^{\mathrm{T}}$ is modeled as random walk. The measurement (18) is obtained at discrete times $t_k, t_{k+1}, t_{k+2}, \ldots$ with a constant time step Δt as $\boldsymbol{y}_k = \boldsymbol{y}(t_k)$. Using this measurement and discretization of (20) yields to

$$\begin{aligned} \boldsymbol{z}_{k+1} &= \boldsymbol{f}_k(\boldsymbol{z}_k, \boldsymbol{a}_k, L) + \boldsymbol{w}_k \\ \boldsymbol{y}_k &= \boldsymbol{h}(\boldsymbol{z}_k) + \boldsymbol{v}_k \end{aligned} \tag{21}$$

where

$$\begin{aligned} \boldsymbol{f}_k(\boldsymbol{z}_k, \boldsymbol{a}_k, L) &= \boldsymbol{z}_k + \boldsymbol{f}(\boldsymbol{z}_k, \boldsymbol{a}_k, L)\Delta t \\ \boldsymbol{h}(\boldsymbol{z}) &= \begin{bmatrix} \phi_x + n_x & \phi_y + n_y \end{bmatrix}^{\mathrm{T}}. \end{aligned} \tag{22}$$

The process and measurement noise are modeled with Gaussian distribution as $\boldsymbol{w}_k \sim \mathcal{N}(0, \boldsymbol{Q})$ and $\boldsymbol{v}_k \sim \mathcal{N}(0, \boldsymbol{R})$ with the covariance matrices $\boldsymbol{Q}$ and $\boldsymbol{R}$. The extended Kalman filter [39] is summarized in Algorithm 1 with transition and observation matrices

$$\boldsymbol{F}_k = \frac{\partial \boldsymbol{f}_k}{\partial \boldsymbol{z}}\Big|_{\hat{\boldsymbol{z}}_k, \boldsymbol{a}_k}, \quad \boldsymbol{H} = \boldsymbol{H}_k = \frac{\partial \boldsymbol{h}}{\partial \boldsymbol{z}}\Big|_{\hat{\boldsymbol{z}}_k}. \tag{23}$$

The pendulum oscillation angles and angular velocities $[\phi_x, \phi_y, \dot{\phi}_x, \dot{\phi}_y]^{\mathrm{T}}$ are then extracted from $\hat{\boldsymbol{z}}_k$.

IV. Cable Length Estimation

In this article, the payload cable length L is assumed to be the distance from the payload suspension point to the center of gravity of the payload.

Modern cranes are equipped with encoders for measuring the length of the released cable L_h down to the hook, however, in practice, the payload is normally suspended from the hook using additional slings or chains, with unknown length L_s, as shown in Fig. 6. In some cases, L_s can be significant in relation to L_h, which means that the total length of the payload cable L in the pendulum model should be found as a sum of both. In this section we present the procedure for estimation of the total cable length L, which is required both in the control law and

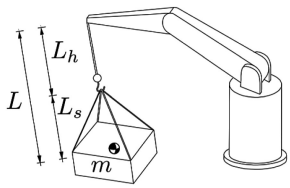

Fig. 6. Total cable length is a sum of crane cable outlet L_h and the effective length of slings L_s.

in the Kalman filter algorithm. We assume that the cable length L is bounded by $L_{\min} \leq L \leq L_{\max}$. In fact, the dynamics of the pendulum in one plane is sufficient to estimate the length of the cable. Therefore, we propose to use only ϕ_x pendulum oscillations.

Provided that ϕ_x is sufficiently small, we can linearize the first equation of (8) about the equilibrium point $(\phi_x, \dot{\phi}_x) = (0, 0)$, which leads to

$$\ddot{\phi}_x = \frac{1}{L^*}(-g\phi_x + \dot{v}_y) \tag{24}$$

where L^* is the true unknown cable length. In our application, its not possible to measure $\ddot{\phi}_x$ and the use of differentiation is not desirable. One way to solve it is to filter both side of (24) with a first-order stable filter $1/\Lambda(s)$, where $\Lambda(s) = s + \lambda_0$ is a Hurwitz polynomial in s. Then the Laplace transformation of (24) yields to the linear parametric model

$$z = \eta^* \psi \tag{25}$$

where $\eta^* = 1/L^*$ and the Laplace transforms of the left-hand and right-hand sides of (24) are

$$z = [\dot{\phi}_x(s)s]/\Lambda(s), \quad \psi = [-g\phi_x(s) + \dot{v}_y(s)]/\Lambda(s). \tag{26}$$

The variables z and ψ can be obtained from the Kalman filter and commanded control input, while the variable η^* is unknown. Consider $\eta(t)$ to be the estimate of η^* at time t, then the estimated value $\hat{z}$ of the output z is obtained as $\hat{z} = \eta\psi$. Since the model (25) is an approximation of the true model (8), we choose a least-square method for estimating η.

We introduce the normalized estimation error

$$\epsilon = (z - \hat{z})/m_s^2 = (z - \eta\psi)/m_s^2 \tag{27}$$

where $m_s^2 = 1 + n_s^2$, the normalizing signal n_s is chosen to be $n_s^2 = \gamma\psi^2$, and γ is a time-varying adaptive gain to be decided. The optimal η should minimize the integral cost function [31], where $\eta \in \mathcal{S}$ and $\mathcal{S} = \{\eta \in \mathbb{R} \mid g(\eta) \leq 0\}$ is a convex set, where $g : \mathbb{R} \to \mathbb{R}$ is a smooth function. If the estimates $\eta(t)$ are bounded by $1/L_{\max} \leq \eta \leq 1/L_{\min}$, then the new variable $\breve{\eta} = \eta - \eta_a$ is bounded by

$$-\bar{\eta} \leq \breve{\eta} \leq \bar{\eta} \tag{28}$$

where $\eta_a = 1/L_{\max} + \bar{\eta}$ and

$$\bar{\eta} = 0.5(L_{\max} - L_{\min})/(L_{\max}L_{\min}). \tag{29}$$

The inequality (28) can be rewritten as $|\breve{\eta}| \leq \bar{\eta}$, which leads to that the inequality $\breve{\eta}^2 - \bar{\eta}^2 \leq 0$ is also satisfied. The inequality $\breve{\eta}^2 - \bar{\eta}^2 \leq 0$ can be explicitly written as

$$\eta^2 - 2\eta\eta_a + \eta_a^2 - \bar{\eta}^2 \leq 0. \tag{30}$$

Provided that $g(\eta)$ should be not greater than zero, then we suggest that the left-hand side of (30) is a reasonable admissible function for $g(\eta)$, that is $g(\eta) = \eta^2 - 2\eta\eta_a + \eta_a^2 - \bar{\eta}^2$, which can alternatively be written as

$$g(\eta) = \eta^2 - \eta\frac{L_{\max} + L_{\min}}{L_{\max}L_{\min}} + \frac{1}{L_{\max}L_{\min}} \tag{31}$$

then the gradient of (31) is defined as

$$\nabla g(\eta) = 2\eta - (L_{\max} + L_{\min})/(L_{\max}L_{\min}). \tag{32}$$

The solution of the constrained minimization problem follows from the least-squares algorithm with projection method and is given by [31]

$$\dot{\eta} = \begin{cases} \gamma\epsilon\psi & \text{if } g(\eta) < 0 \\ & \text{or if } g(\eta) = 0 \text{ and } (\gamma\epsilon\psi)\nabla g(\eta) \leq 0 \\ 0 & \text{otherwise} \end{cases} \tag{33}$$

where the derivative of the time-varying adaptive gain is given by

$$\dot{\gamma} = \begin{cases} \beta\gamma - \gamma^2\psi^2/m_s^2 & \text{if } g(\eta) < 0 \\ & \text{or if } g(\eta) = 0 \text{ and } (\gamma\epsilon\psi)\nabla g(\eta) \leq 0 \\ 0 & \text{otherwise.} \end{cases} \tag{34}$$

The initial guess of the pendulum length $L_0 = 1/\eta_0$ should satisfy $L_{\min} \leq 1/\eta_0 \leq L_{\max}$. The performance of the cable length estimation algorithm is studied by the experiment. The estimate of the cable length $L = 1/\eta$ is used in the control problem and the extended Kalman filter. The initial value of γ is chosen to be $\gamma_0 > 0$, the forgetting factor is $\beta > 0$ and the initial value of η is η_0.

V. Control

The controller is derived for the acceleration of the crane tip since it is the input for the spherical pendulum dynamics in (8). The designed acceleration is used as input for both the control of the crane, the cable length estimation algorithm and the extended Kalman filter (EKF). Our goal is to control both the crane tip position (x_5, y_5) and the pendulum oscillation angles (ϕ_x, ϕ_y) with the control input $(\ddot{x}_5, \ddot{y}_5)$. In order to avoid large pendulum oscillation angles, the pendulum oscillation angles should be controlled with a high bandwidth. It is assumed that it is less necessary to control the suspension point position equally fast. Therefore, the controller was designed with a payload damping controller in an inner loop with high bandwidth, and a controller for the crane tip position in an outer loop with lower bandwidth. We propose a controller

$$\ddot{x}_5 = 2L\zeta\omega_0\dot{\phi}_y + u_x, \quad \ddot{y}_5 = -2L\zeta\omega_0\dot{\phi}_x + u_y \tag{35}$$

with feedback from the angular rates $\dot{\phi}_x$ and $\dot{\phi}_y$, where the acceleration $(\ddot{x}_5, \ddot{y}_5)$ of the crane tip in the horizontal plane is the control variable, and u_x and u_y are the control variables of the

outer control loop. Implementation issues related to the use of acceleration for the control variables are discussed at the end of this section. The closed-loop dynamics of the payload linearized about $(\phi_x, \phi_y, \dot{\phi}_x, \dot{\phi}_y) = \mathbf{0}$ are found from (8) and (35) to be

$$\begin{aligned} \ddot{\phi}_x + 2\zeta\omega_0\dot{\phi}_x + \omega_0^2\phi_x &= u_y/L \\ \ddot{\phi}_y + 2\zeta\omega_0\dot{\phi}_y + \omega_0^2\phi_y &= -u_x/L. \end{aligned} \tag{36}$$

It is seen that in a special case when $(u_x, u_y) = (0, 0)$ the linearized closed-loop system is two harmonic oscillators with undamped natural frequency ω_0 and relative damping ζ. In a general case when (u_x, u_y) are not necessarily zero, the Laplace transform of the closed-loop dynamics (36) gives

$$\phi_x(s) = G(s)u_y(s), \quad \phi_y(s) = -G(s)u_x(s) \tag{37}$$

where the transfer function $G(s)$ is

$$G(s) = \frac{1}{L(s^2 + 2\zeta\omega_0 s + \omega_0^2)}. \tag{38}$$

Insertion of (37) into the Laplace transform of (35) gives

$$x_5(s) = \frac{H(s)}{s^2}u_x(s), \quad y_5(s) = \frac{H(s)}{s^2}u_y(s) \tag{39}$$

where

$$H(s) = 1 - 2L\zeta\omega_0 sG(s) = \frac{s^2 + \omega_0^2}{s^2 + 2\zeta\omega_0 s + \omega_0^2}. \tag{40}$$

For frequencies $\omega \ll \omega_0$, it follows that $H(j\omega) \to 1$ and (39) simplifies to

$$x_5(s) = \frac{1}{s^2}u_x(s), \quad y_5(s) = \frac{1}{s^2}u_y(s). \tag{41}$$

The position of the crane tip can be controlled with a proportional derivative (PD) controller

$$\begin{aligned} u_x &= k_p(x_d - x_5) + k_d(\dot{x}_d - \dot{x}_5) \\ u_y &= k_p(y_d - y_5) + k_d(\dot{y}_d - \dot{y}_5) \end{aligned} \tag{42}$$

where $\boldsymbol{p}_{05}^0 = [x_5, y_5, z_5]^{\mathrm{T}}$ is the position of the crane tip relative to the inertial frame and (x_d, y_d) is the desired position of the crane tip. The gains can be selected as $k_p = w_s^2$ and $k_d = 2\zeta_s\omega_s$, where $\omega_s \ll \omega_0$ and ζ_s can be selected in the range [0.7,1]. The condition $\omega_s \ll \omega_0$ should be sufficiently well satisfied if $\omega_s = \omega_0/k_s$, where $k_s \geq 5$ and ω_s is the bandwidth in the outer loop.

In practice, it will not be possible to command the acceleration of the crane tip. The solution is to command the velocity instead, as the crane used in the experiments and most industrial cranes will have velocity control with the desired velocity is input variable. Therefore, the acceleration input was converted to velocity inputs, as described in [40]. This was done by integrating the two acceleration commands $\ddot{x}_5$ and $\ddot{y}_5$ in (35) to velocity commands w_x and w_y, and then using w_x and w_y as inputs to the velocity loops given by

$$\dot{w}_x = \ddot{x}_5, \quad \dot{w}_y = \ddot{y}_5 \tag{43}$$

$$\dot{v}_x = \frac{1}{T_v}(w_x - v_x), \quad \dot{v}_y = \frac{1}{T_v}(w_y - v_y). \tag{44}$$

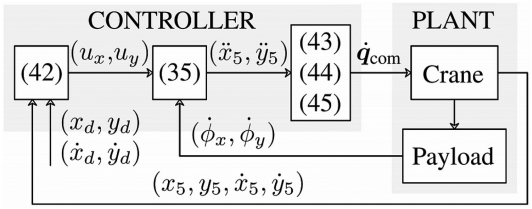

Fig. 7. Block diagram of the cascade controller and velocity loops, where the numbers inside the blocks indicate the equation numbers.

If the bandwidth $1/T_v$ of the velocity loop is sufficiently fast compared to the bandwidth of the damping controller, the resulting velocities v_y and v_y will be close to the velocity commands w_x and w_y, and it follows that the accelerations $\ddot{x}_5$ and $\ddot{y}_5$ will be sufficiently close to the commanded accelerations $\dot{v}_x$ and $\dot{v}_y$. The commanded velocities v_x and v_y are further transformed to the crane joint space according to

$$\dot{\boldsymbol{q}}_{\mathrm{com}} = \boldsymbol{J}^{-1}\begin{bmatrix} v_x & v_y & 0 \end{bmatrix}^{\mathrm{T}} \tag{45}$$

where the Jacobian $\boldsymbol{J}$ is given in (7) and $\dot{\boldsymbol{q}}_{\mathrm{com}}$ is the commanded joint velocities of the crane. A block diagram of the controller presented in this chapter is given in Fig. 7.

VI. Experimental Results

The performance of the proposed mechatronic system was evaluated in laboratory experiments. A setup with a scaled knuckle boom crane was designed and constructed. The crane setup is shown in Fig. 2. The crane was driven by one servo motor and two electro-mechanical cylinders driven by servo motors. All servo motors were equipped with encoders for measuring angles and angular velocities. The vision-based sensor system consisted of three consumer-grade web cameras, where the resolution was selected as 1280×720 pixels. The distance between the cameras was $\delta_{12} = \delta_{23} = 0.24\mathrm{m}$, and the spherical markers had a diameter of $0.03\mathrm{m}$. The control hardware consisted of a personal computer (PC) and a programmable logic controller (PLC). The PLC was used to read the data from the motor encoders and send commands to the servo drives to control the servo motor. The PC was used for computation and communication with the PLC. The measurements of $\boldsymbol{q}_c$ and $\dot{\boldsymbol{q}}_c$ were obtained from the PLC.

For the software part, MATLAB/Simulink was used on the PC for running the controller and the cable length estimation algorithm, while Python with OpenCV was used for the vision calculations and the extended Kalman filter. The control period was set to 50 ms. The communication between MATLAB/Simulink and Python was implemented with socket programming with user datagram protocol (UDP). The full overview of the signals in the system is given in Fig. 8. The covariance of the process noise in the extended Kalman filter was $\boldsymbol{Q} = 10^{-4}\mathrm{diag}(0.3, 0.3, 5, 5, 1, 1)$ and the covariance of the measurement noise was

$$\boldsymbol{R} = 10^{-3}\begin{bmatrix} 3.77597 & -2.10312 \\ -2.10312 & 1.25147 \end{bmatrix}.$$

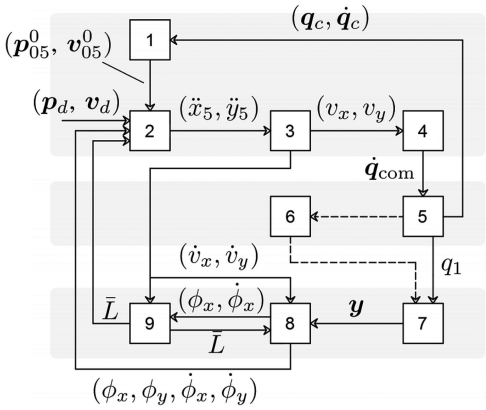

Fig. 8. Flow chart of the vision-based controller where (1) is the forward kinematics and Jacobian, (2) is the controller, (3) is the velocity loop, (4) is the inverse of the Jacobian, (5) is the physical crane, (6) is the physical payload, (7) is the vision system, (8) is the extended Kalman filter, and (9) is the cable length estimation.

The covariance matrix $\boldsymbol{R}$ was obtained by calculating the covariance between two vectors containing a number of stored values of the measurements y_1 and y_2, which was followed by some manual tuning. These two vectors were obtained while the pendulum was kept vertical. The covariance matrix $\boldsymbol{Q}$ was manually tuned with $\boldsymbol{R}$ kept fixed. The initial *a posteriori* state was $\hat{\boldsymbol{z}}_0 = \boldsymbol{0}$ and the error covariance matrix was $\hat{\boldsymbol{P}}_0 = \boldsymbol{0}$.

The forgetting factor in the cable length estimation algorithm was $\beta = 0.5$, and the initial adaptive gain was $\gamma(0) = 100$.

A. Cable Length Estimation

The performance of the cable length estimation algorithm was studied in an experiment where the payload was oscillating, while the crane tip position was stationary. The true cable length, which is the distance from the suspension point to the center of gravity of the payload, was $L^* = 1.05$ m. In the experiments, the payload was excited by manually applying initial displacements of different magnitude. During the experiment the amplitude of the oscillations was naturally damped by a few degrees. The estimated cable length L and the low-pass filtered estimate $\bar{L}$ were logged in the experiments, where the low-pass filtered estimate $\bar{L}$ of the cable length was used as an input to the extended Kalman filter. In all the tests, the estimate of the cable length L was bounded by $L_{\min} = 0.3$m and $L_{\max} = 1.5$ m.

In the first run, the initial amplitude of the payload oscillations was $\phi_x = 15^\circ$ and the initial cable length guess was $L_0 = 0.5$ m. The estimate of the cable length converged in less than 10 s, as shown in Fig. 9(a). Next, an experiment with the initial angle $\phi_x = 0.5^\circ$ was performed. In this case, the estimate of the length was more sensitive to noise, and the estimate oscillated between 0.75 and 1.5 m after the initial convergence, as shown in Fig. 9(b). The reason for the loss of performance in this case is that the input data to the adaptive algorithm were not persistently exciting [31] to achieve high quality of the estimates. More tests were run with the initial angles of 5° and 20°, and the initial cable length guesses of 0.5, 0.7, and 1.4 m. In these cases, only the filtered cable length estimates were plotted in Fig. 10.

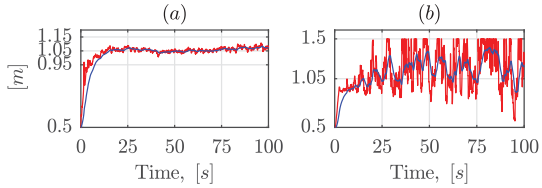

Fig. 9. Estimation of the cable length with different pendulum oscillation angles ϕ_x : (a) $|\phi_x| < 15^\circ$ and (b) $|\phi_x| < 0.5^\circ$. The red lines show the estimate L and the blue lines show $\bar{L}$ the estimate processed by a low-pass filter. The initial guess is $L_0 = 0.5$m, and the true length is $L^* = 1.05$m.

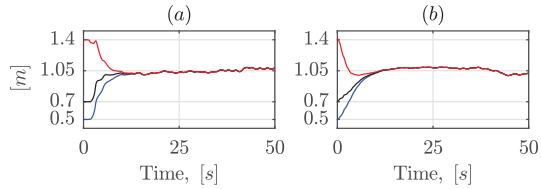

Fig. 10. Filtered estimates of the cable length with different initial guesses: (a) $|\phi_x| < 5^\circ$ and (b) $|\phi_x| < 20^\circ$. The true length is $L^* = 1.05$ m. The red, black and blue lines correspond to the initial length guesses $L = 1.4$m, $L = 0.7$m and $L = 0.5$m, respectively.

The experimental results shown in Figs. 9 and 10 demonstrate that the cable length estimate was converging to the true length $L^* = 1.05$m after approximately 10 s in all the presented cases, except for the case [see Fig. 9 (b)] with close-to-zero payload oscillations. It is seen that for small payload oscillation angles the estimate was noisier, as in Fig. 10(a), which could happen due to that the Kalman filter estimates were noisier for small angles. For large payload oscillations, as in Fig. 10(b), the estimate deviated more from the true value, which could happen due to that the linearized pendulum model was used for the cable length estimation algorithm. As expected, the cable length failed to converge when the payload did not oscillate. It is suggested that the cable length should be estimated *before* the controller starts damping the payload motion. It is feasible in practice because in most of the cases the crane operator would do a manual maneuver before reaching the desired crane tip position over the landing site, then the payload motion can be damped right before the payload landing.

B. Crane Control

The performance of the crane controller was investigated in an experiment that represented a realistic hoisting operation, where a payload is first carried over a landing site, and then the payload oscillations are damped out so that the payload can be landed safely. The experiment was executed in the following order. The crane tip was initially at the position $\boldsymbol{p}_{05}^0 = [1.27, 1.27]$ m, and the payload was manually excited. Then at $t = 1$ s, the desired crane tip position was set to $\boldsymbol{p}_d = [0.70, 1.80]$ m, and the crane moved to the desired position and finished the maneuver at $t = 12$ s. The controller for payload damping was turned off during this maneuver. At time $t = 20$ s, the payload damping controller was turned ON. The cable length was estimated throughout the whole experiment until the damping controller was turned ON at $t = 20$ s, then the estimate was frozen, see the discussion

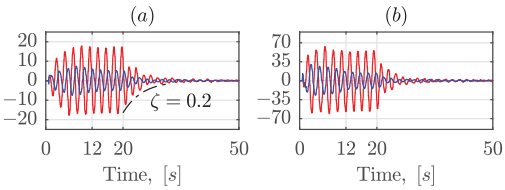

Fig. 11. Experimental results with $\zeta = 0.2$. (a) Orientation angles in [deg] and (b) angular velocities in [deg/s]. Red lines show ϕ_x, $\dot{\phi}_x$, and blue lines show ϕ_y, $\dot{\phi}_y$. The dashed line is a theoretical exponential decay curve.

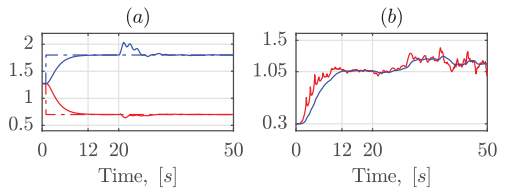

Fig. 12. Experimental results with $\zeta = 0.2$. (a) Crane tip position relative to the inertia frame in [m], red lines show x, x_d, and blue lines show y, y_d. (b) Cable length estimate in [m], original estimate (in red), and filtered estimate (in blue).

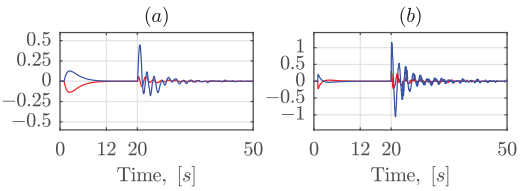

Fig. 13. Experimental results with $\zeta = 0.2$. (a) Commanded velocities of the crane tip in [m/s] and (b) control accelerations of the crane tip in [m/s^2]. Red lines show v_x, $\dot{v}_x$, and blue lines show v_y, $\dot{v}_y$.

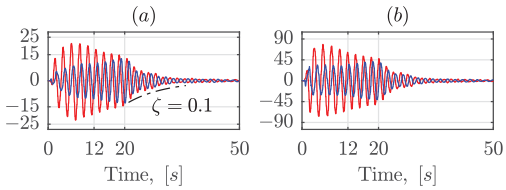

Fig. 14. Experimental results with $\zeta = 0.1$. (a) Orientation angles in [deg] and (b) angular velocities in [deg/s]. Red lines show ϕ_x, $\dot{\phi}_x$, and blue lines show ϕ_y, $\dot{\phi}_y$. The dashed line is a theoretical exponential decay curve.

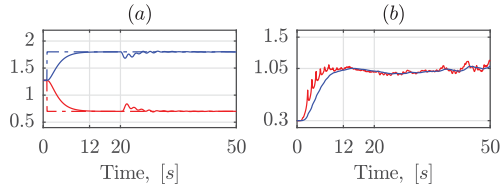

Fig. 15. Experimental results with $\zeta = 0.1$. (a) Crane tip position relative to the inertia frame in [m], red lines show x, x_d, and blue lines show y, y_d. (b) Cable length estimate in [m], original estimate (in red), and filtered estimate (in blue).

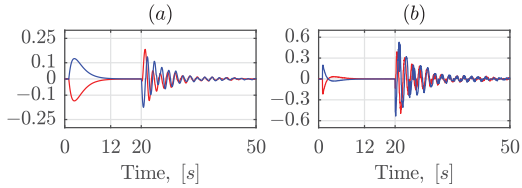

Fig. 16. Experimental results with $\zeta = 0.1$. (a) Commanded velocities of the crane tip in [m/s] and (b) control accelerations of the crane tip in [m/s^2]. Red lines show v_x, $\dot{v}_x$, and blue lines show v_y, $\dot{v}_y$.

in Section VI-A. The initial estimate of the cable length was set to $L_0 = 0.3\text{m}$ (far off the true cable length) to illustrate the performance of the adaptive parameter estimation algorithm. The bandwidth in the outer control loop was selected as $\omega_s = \omega_0/5$, and the relative damping ratio was selected as $\zeta_s = 1$. Two different values 0.1 and 0.2 were used for the relative damping ratio ζ in the inner loop.

The experimental results with the relative damping ratio $\zeta = 0.2$ are given in Figs. 11–13. The values of the estimated payload orientation angles and angular velocities are shown in Fig. 11. The values of the measured crane tip position relative to the inertial frame and given in the coordinates of the inertial frame, as well as the estimates of the cable length are given in Fig. 12. The control acceleration and commanded velocities of the crane tip are given in Fig. 13.

The same types of experimental results with the relative damping ratio $\zeta = 0.1$ are given in Figs. 14–16.

Given the results in Figs. 11 and 14, the payload oscillations were controlled correctly with a decay of the oscillations close to the theoretical exponential decay curve for all tested ζ cases. In addition, the results in Figs. 12 and 15 show that the position of the crane tip was also controlled correctly, that is it eventually converged to the desired value. Both observations above let us conclude that the proposed cascade controller was efficient in all tested cases. The performance of the controller could be predicted by theoretical exponential decay curves. The performance of the proposed procedure for the cable length estimation can be evaluated from the results in Figs. 12 and 15. It is noted that in contrast with the results in Fig. 10, here the oscillations were not free, that is the control acceleration was fed to the algorithm. In all tested cases, the estimate of the cable length converged to the true value $L^* = 1.05\text{m}$ after 12 s and until the time $t = 20$ s the maximum error was 4.0%. As expected (see Section VI-A), poorer convergence was demonstrated after the payload motion started being damped out at $t > 20$ s.

In order to compare the proposed cascade controller with another solutions, a closed-loop controller and an open-loop controller are implemented for the knuckle boom crane. The considered closed-loop controller is the well-known LQR method [41] and the considered open-loop controller is the robust EI input shaper [42]. Both controllers were derived based on a linear spherical pendulum model with known cable length which was obtained by linearizing the spherical pendulum dynamics (8) around the equilibrium point. The EI shaper was designed with a tolerable level of vibration chosen as 1%. For the LQR method with a cost function $\int_0^\infty (\boldsymbol{X}^{\mathrm{T}}\bar{\boldsymbol{Q}}\boldsymbol{X} + \boldsymbol{u}^{\mathrm{T}}\bar{\boldsymbol{R}}\boldsymbol{u})dt$, where $\boldsymbol{u} = [\dot{v}_x, \dot{v}_y]^{\mathrm{T}}$ and $\boldsymbol{X} = [\phi_x, \phi_y, \dot{\phi}_x, \dot{\phi}_y, x_5 - x_d, y_5 - y_d, \dot{x}_5 - \dot{x}_d, \dot{y}_5 - \dot{y}_d]^{\mathrm{T}}$, the optimal feedback control law $\boldsymbol{u} = -\boldsymbol{K}\boldsymbol{X}$ that minimizes the cost function, was obtained by using

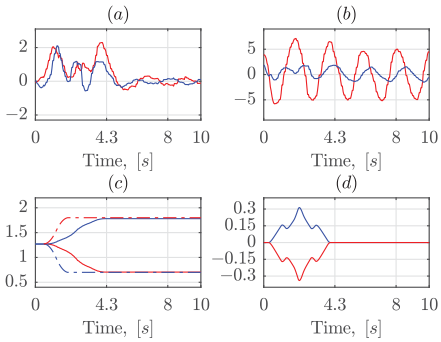

Fig. 17. Experimental results for the EI shaper. (a) Orientation angles in [deg] with zero initial orientation angles and (b) orientation angles in [deg] with nonzero initial orientation angles, where red lines show ϕ_x and blue lines show ϕ_y. (c) Crane tip position relative to the inertia frame in [m], red lines show x, x_d and blue lines show y, y_d. (d) Commanded velocities of the crane tip in [m/s], red line shows v_x and and blue line shows v_y.

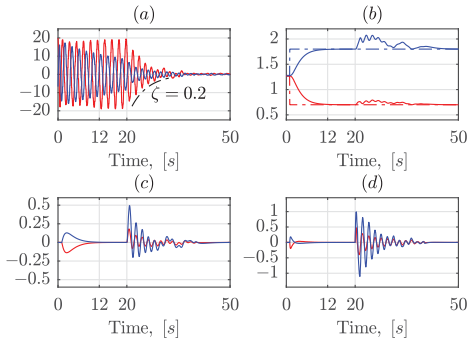

Fig. 18. Experimental results for the LQR method. (a) Orientation angles in [deg], red line shows ϕ_x and blue line shows ϕ_y. (b) Crane tip position relative to the inertia frame in [m], red lines show x, x_d and blue lines show y, y_d. (c) Commanded velocities of the crane tip in [m/s], red line shows v_x and and blue line shows v_y. (d) Control accelerations of the crane tip in [m/s^2], red line shows $\dot{v}_x$ and blue line shows $\dot{v}_y$.

the MATLAB function `lqr`. After careful tuning and test runs on the knuckle boom crane, we choose the matrices $\bar{\boldsymbol{R}} = \text{diag}(5, 5)$ and $\bar{\boldsymbol{Q}} = \text{diag}(1, 1, 9.2, 9.2, 0.72, 0.72, 2.5, 2.5)$.

The obtained experimental results from the EI shaper and LQR method, are illustrated in Figs. 17 and 18, respectively. It is seen that in the case of zero initial pendulum oscillations, the EI method provided robust control of both the crane tip position and pendulum oscillations. However, in the case of non-zero initial pendulum oscillations, the EI method gave obvious residual pendulum oscillations, which is expected for an open-loop controller.

For the LQR method, the pendulum damping was tuned to be similar to the proposed cascade controller with relative damping $\zeta = 0.2$, see Figs. 11 and 18. However, the proposed controller had a better convergence for the crane tip position, as well as the deviation from the crane tip set point was smaller, see Figs. 12 and 18. Its worth noting that the LQR controller requires to perform a new optimization for every new estimate of the cable length L, which is more computationally demanding than the length update in the proposed controller. In addition, the LQR weight matrices, $\bar{\boldsymbol{R}}$ and $\bar{\boldsymbol{Q}}$, are less intuitive and it is difficult to predict the resulting pendulum damping without testing. For the proposed controller the exponential decay ratio ζ is given as a tuning parameter, which can be directly used for predicting the pendulum damping.

VII. Conclusion

In this article, we have presented a vision-based control system for a knuckle boom crane with online payload cable length estimation. The estimation of the payload oscillations was done using an extended Kalman filter with input from a visual sensor configuration that is novel for crane control. This visual sensor consisted of three 2-D cameras rigidly attached to the crane king, which were tracking the position of two spherical markers on the payload cables. The markers were identified using the size and color information, where the color was selected to stand out from typical colors in the laboratory. No special background was used during the experiments, and the markers were always correctly identified even when the background was unstructured laboratory equipment. The cable length estimation procedure was experimentally studied both for the case of free payload oscillations and for the case of forced oscillations. The convergence of the estimate was achieved with minor errors in all the cases, except for the case with close-to-zero oscillations, which was expected. The performance of the linear cascade controller designed was experimentally verified using the realistic payload geometry and configuration. The experiments were conducted for two cases with the damping factor of $\zeta = 0.2$ and $\zeta = 0.1$. The controller efficiently damped out the payload oscillations, while the crane tip position converged to the desired position in all the conducted experiments. The decay of the payload oscillations was very close to the theoretical exponential decay curves. The proposed controller was experimentally compared to the LQR and robust EI methods. The proposed controller demonstrated superior performance over the open-loop robust EI shaper, as it was expected. Compared to the LQR controller, the proposed method demonstrated a better crane tip conversion for the similar pendulum damping ratio. In addition, the proposed controller is less computationally demanding, as it does not require a new optimisation for every new estimate of the cable length.

References

[1] E. M. Abdel-Rahman, A. H. Nayfeh, and Z. N. Masoud, "Dynamics and control of cranes: A review," *Modal Anal.*, vol. 9, no. 7, pp. 863–908, 2003.

[2] L. Ramli, Z. Mohamed, A. M. Abdullahi, H. Jaafar, and I. M. Lazim, "Control strategies for crane systems: A comprehensive review," *Mech. Syst. Signal Process.*, vol. 95, no. C, pp. 1–23, 2017.

[3] D. Blackburn, J. Lawrence, J. Danielson, W. Singhose, T. Kamoi, and A. Taura, "Radial-motion assisted command shapers for nonlinear tower crane rotational slewing," *Control Eng. Pract.*, vol. 18, no. 5, pp. 523–531, 2010.

[4] D. Kim and W. Singhose, "Performance studies of human operators driving double-pendulum bridge cranes," *Control Eng. Pract.*, vol. 18, no. 6, pp. 567–576, 2010.

[5] J. Yu, F. L. Lewis, and T. Huang, "Nonlinear feedback control of a gantry crane," in *Proc. Amer. Control Conf.*, vol. 6, Jun. 1995, pp. 4310–4315.

[6] K. Yoshida, "Nonlinear controller design for a crane system with state constraints," in *Proc. Amer. Control Conf. (IEEE Cat. No.98CH36207)*, Jun. 1998, vol. 2, pp. 1277–1283.

[7] T. Vyhldal, M. Anderle, J. Buek, and S. Niculescu, "Time-delay algorithms for damping oscillations of suspended payload by adjusting the cable length," *IEEE/ASME Trans. Mechatronics*, vol. 22, no. 5, pp. 2319–2329, Oct. 2017.

[8] N. Sun, Y. Fang, H. Chen, and B. He, "Adaptive nonlinear crane control with load hoisting/lowering and unknown parameters: Design and experiments," *IEEE/ASME Trans. Mechatronics*, vol. 20, no. 5, pp. 2107–2119, Oct. 2015.
[9] A. Cibicik, T. A. Myhre, and O. Egeland, "Modeling and control of a bifilar crane payload," in *Proc. Annu. Amer. Control Conf.*, 2018, pp. 1305–1312.
[10] Z. Wu, X. Xia, and B. Zhu, "Model predictive control for improving operational efficiency of overhead cranes," *Nonlinear Dyn.*, vol. 79, no. 4, pp. 2639–2657, 2015.
[11] M. Vukov, W. V. Loock, B. Houska, H. Ferreau, J. Swevers, and M. Diehl, "Experimental validation of nonlinear MPC on an overhead crane using automatic code generation," in *Proc. Amer. Control Conf.*, 2012, pp. 6264–6269.
[12] E. Arnold, O. Sawodny, J. Neupert, and K. Schneider, "Anti-sway system for boom cranes based on a model predictive control approach," in *Proc. IEEE Int. Conf. Mechatronics Autom.*, Jul. 2005, vol. 3, pp. 1533–1538.
[13] J. Neupert, E. Arnold, K. Schneider, and O. Sawodny, "Tracking and anti-sway control for boom cranes," *Control Eng. Pract.*, vol. 18, no. 1, pp. 31–44, 2010.
[14] K. Zhang, J. Chen, Y. Li, and Y. Gao, "Unified visual servoing tracking and regulation of wheeled mobile robots with an uncalibrated camera," *IEEE/ASME Trans. Mechatronics*, vol. 23, no. 4, pp. 1728–1739, Aug. 2018.
[15] S. Hutchinson, G. D. Hager, and P. I. Corke, "A tutorial on visual servo control," *IEEE Trans. Robot. Autom.*, vol. 12, no. 5, pp. 651–670, Oct. 1996.
[16] B. Espiau, F. Chaumette, and P. Rives, "A new approach to visual servoing in robotics," *IEEE Trans. Robot. Autom.*, vol. 8, no. 3, pp. 313–326, Jun. 1992.
[17] B. Thuilot, P. Martinet, L. Cordesses, and J. Gallice, "Position based visual servoing: Keeping the object in the field of vision," in *Proc. IEEE Int. Conf. on Robot. Autom. (Cat. No.02CH37292)*, May 2002, vol. 2, pp. 1624–1629.
[18] F. Janabi-Sharifi, L. Deng, and W. J. Wilson, "Comparison of basic visual servoing methods," *IEEE/ASME Trans. Mechatronics*, vol. 16, no. 5, pp. 967–983, Oct. 2011.
[19] A. Chiuso, P. Favaro, H. Jin, and S. Soatto, "Structure from motion causally integrated over time," *IEEE Trans. Pattern Anal. Mach. Intell.*, vol. 24, no. 4, pp. 523–535, Apr. 2002.
[20] G. Panahandeh and M. Jansson, "Vision-aided inertial navigation based on ground plane feature detection," *IEEE/ASME Trans. Mechatronics*, vol. 19, no. 4, pp. 1206–1215, Aug. 2014.
[21] J. Weng, N. Ahuja, and T. S. Huang, "Optimal motion and structure estimation," *IEEE Trans. Pattern Anal. Mach. Intell.*, vol. 15, no. 9, pp. 864–884, Sep. 1993.
[22] F. Pereira, J. Luft, G. Ilha, and A. Susin, "A novel resection-intersection algorithm with fast triangulation applied to monocular visual odometry," *IEEE Trans. Intell. Transp. Syst.*, vol. 19, no. 11, pp. 3584–3593, Nov. 2018.
[23] R. I. Hartley and A. Zisserman, *Multiple View Geometry in Computer Vision*, 2nd ed., Cambridge, U.K.: Cambridge Univ. Press, 2004.
[24] D. Scharstein and R. Szeliski, "A taxonomy and evaluation of dense two-frame stereo correspondence algorithms," *Int. J. Comput. Vis.*, vol. 47, pp. 7–42, 2002.
[25] M. Z. Brown, D. Burschka, and G. D. Hager, "Advances in computational stereo," *IEEE Trans. Pattern Anal. Mach. Intell.*, vol. 25, no. 8, pp. 993–1008, Aug. 2003.
[26] B. Tippetts, D. J. Lee, K. Lillywhite, and J. Archibald, "Review of stereo vision algorithms and their suitability for resource-limited systems," *J. Real-Time Image Process.*, vol. 11, no. 1, pp. 5–25, Jan. 2016.
[27] H. Stewenius, F. Schaffalitzky, and D. Nister, "How hard is 3-view triangulation really?" *IEEE Int. Conf. Comput. Vis.*, 2005, vol. 1, pp. 686–693.
[28] Z. Kukelova, T. Pajdla, and M. Bujnak, "Fast and stable algebraic solution to L2 three-view triangulation," in *Proc. Int. Conf. 3D Vis. Comp. Soc.*, 2013, pp. 326–333.
[29] J. Hedborg, A. Robinson, and M. Felsberg, "Robust three-view triangulation done fast," in *Proc. IEEE Conf. Comput. Vis. Pattern Recognit. Workshops*, Jun. 2014, pp. 152–157.
[30] S. Sastry and M. Bodson, *Adaptive Control: Stability, Convergence, and Robustness*. Upper Saddle River, NJ, USA: Prentice-Hall, 1989.
[31] P. A. Ioannou and J. Sun, *Robust Adaptive Control*. Mineola, NY, USA: Courier Dover Publications, 2012.
[32] G. Kenne, T. Ahmed-Ali, F. Lamnabhi-Lagarrigue, and A. Arzande, "Nonlinear systems time-varying parameter estimation: Application to induction motors," *Elect. Power Syst. Res.*, vol. 78, no. 11, pp. 1881–1888, 2008.
[33] J. Na, J. Yang, X. Ren, and Y. Guo, "Robust adaptive estimation of nonlinear system with time-varying parameters," *Int. J. Adaptive Control Signal Process.*, vol. 29, no. 8, pp. 1055–1072, 2015.
[34] V. Lertpiriyasuwat and M. C. Berg, "Adaptive real-time estimation of end-effector position and orientation using precise measurements of end-effector position," *IEEE/ASME Trans. Mechatronics*, vol. 11, no. 3, pp. 304–319, Jun. 2006.
[35] J. Shin, K. Kwak, S. Kim, and H. J. Kim, "Adaptive range estimation in perspective vision system using neural networks," *IEEE/ASME Trans. Mechatronics*, vol. 23, no. 2, pp. 972–977, Apr. 2018.
[36] O. Sawodny, H. Aschemann, J. Kumpel, C. Tarin, and K. Schneider, "Anti-sway control for boom cranes," in *Proc. Amer. Control Conf. (IEEE Cat. No. CH37301)*, May 2002, vol. 1, pp. 244–249.
[37] B. Siciliano, L. Sciavicco, L. Villani, and G. Oriolo, *Robotics: Modelling, Planning and Control*, 1st ed. New York, NY, USA: Springer, 2008.
[38] G. O. Tysse and O. Egeland, "Crane load position control using Lyapunov-based pendulum damping and nonlinear MPC position control," in *Proc. 18th Eur. Control Conf.*, Jun. 2019, pp. 1628–1635.
[39] R. Brown and P. Hwang, *Introduction to Random Signals and Applied Kalman Filtering With Matlab Exercises*. Hoboken, NJ, USA: Wiley, 2012.
[40] F. Rauscher, S. Nann, and O. Sawodny, "Motion control of an overhead crane using a wireless hook mounted IMU," in *Proc. Annu. Amer. Control Conf.*, 2018, pp. 5677–5682.
[41] N. Sun, Y. Fang, H. Chen, B. Lu, and Y. Fu, "Slew/translation positioning and swing suppression for 4-DoF tower cranes with parametric uncertainties: Design and hardware experimentation," *IEEE Trans. Ind. Electron.*, vol. 63, no. 10, pp. 6407–6418, Oct. 2016.
[42] J. Vaughan, A. Yano, and W. Singhose, "Comparison of robust input shapers," *J. Sound Vib.*, vol. 315, no. 4, pp. 797–815, 2008.

Geir Ole Tysse (Member, IEEE) received the M.Sc. degree in subsea technology from the Norwegian University of Science and Technology (NTNU), Trondheim, Norway, in 2015. He is currently working toward the Ph.D. degree in production systems with the Department of Mechanical and Industrial Engineering, NTNU.

His research interests include vision and estimation theory, robotics, control systems, mathematical modeling of rigid multibody systems, and dynamics of marine vessels.

Andrej Cibicik (Member, IEEE) received the M.Sc. degree in civil engineering from the Technical University of Denmark (DTU), Copenhagen, Denmark, in 2012. He is currently working toward the Ph.D. degree in mechanical engineering with the Department of Mechanical and Industrial Engineering, Norwegian University of Science and Technology, Trondheim, Norway.

From 2012 to 2016, he held industrial positions within structural strength analysis of civil structures and offshore drilling equipment. His research interests include robotics, mathematical modeling of rigid and flexible multibody systems, automatic control, sensor systems, and estimation.

Olav Egeland (Senior Member, IEEE) received the M.Sc. and Ph.D. degrees in automatic control from the Norwegian University of Science and Technology (NTNU), Trondheim, Norway, in 1984 and 1987, respectively.

He was a Professor of automatic control with NTNU from 1989 to 2004, and the Co-founder of a start-up from 2004 to 2011. He is currently a Professor of production automation with the NTNU. His research interests include mathematical modeling, robotic production, and offshore control systems.

Dr. Egeland was the Recipient of the Automatica Prize Paper Award in 1996 and the IEEE TRANSACTIONS ON CONTROL SYSTEM TECHNOLOGY Outstanding Paper Award in 2000. He was an Associate Editor of the IEEE TRANSACTIONS ON AUTOMATIC CONTROL from 1996 to 1999 and the *European Journal of Control* from 1998 to 2000.